ADVANCED MATERIALS
www.advmat.de

Construction of Active Protein Materials: Manipulation on Morphology of Salmon Calcitonin Assemblies with Enhanced Bone Regeneration Effect

Libin Wu, Liang Cheng, Jing Yang, Yufei Yan, Ensong Zhang, Zdravko Kochovski, Long Li, Zhen Wang, Lianfu Deng, Yan Lu, Pol Besenius, Wenguo Cui, and Guosong Chen**

The effect of protein drugs is always limited by their relatively low stability and fast degradation property; thus, various elegant efforts have been made to improve the bioactivity and biocompatibility of the protein drugs. Here, an alternative way is proposed to solve this problem. By simply adding a limited amount of small-molecular regulator, which tunes the subtle balance of protein–protein interactions (PPIs) and disulfide bond formation, the self-assembly property of the protein drug can be regulated, forming an "active protein material" itself. This means that, the resulting biomaterial is dominated by the protein drug and water, with significantly enhanced bone regeneration effect compared to the virgin protein in vitro and in vivo, through multivalent effect between the protein and receptor and the retarded degradation of the assembled proteins. In this active protein material, the protein drug is not only the active drug, but also the drug carrier, which greatly increases the drug-loading efficiency of the biomaterial, indicating the advantages of the easy preparation, high efficiency, and low cost of the active protein material with a bright future in biomedical applications.

1. Introduction

Proteins are nature's versatile building blocks for organisms with sophisticated topological structures and broad spectrum of functions.[1] Protein assemblies are structures with regular patterns formed by proteins at nanometer and micrometer scales, which not only are easily found in nature as virus capsid and microtubules, but also can be made by scientists in laboratories.[2-4] The programmable self-assembly of proteins into controllable nanostructures creates lots of possibilities for innovative bionanomaterials construction.[5] Generally, the self-assembly of proteins is manipulated by the meticulous design of protein–protein interactions (PPIs) by biological technologies. Recently, with the advancements in supramolecular chemistry, chemical strategies have made it possible to further control the thermodynamics and kinetics of the protein self-assembly process. Various supramolecular interactions, such as metal-ion, dipolar, or van der Waals interactions of large apolar surfaces, have been employed to construct well-organized protein nanoarchitectures.[6–8] The research field attracts increasing attention, because the resulting protein assemblies are believed to have promising functions and practical applications in nanodevices, biocatalysts, drug delivery, etc.[9–11]

In the research field of protein assembly, structural control on the assembly morphology and packing pattern has been developed to such an unprecedented level.[4,12] However, the

---

L. Wu, J. Yang, E. Zhang, L. Li, G. Chen
The State Key Laboratory of Molecular Engineering of Polymers
and Department of Macromolecular Science
Fudan University
Shanghai 200433, P. R. China
E-mail: guosong@fudan.edu.cn

L. Cheng, Y. Yan, Z. Wang, L. Deng, W. Cui
Department of Orthopaedics
Shanghai Key Laboratory for Prevention and Treatment of Bone
and Joint Diseases
Shanghai Institute of Traumatology and Orthopaedics
Ruijin Hospital
Shanghai Jiao Tong University School of Medicine
197 Ruijin 2nd Road, Shanghai 200025, P. R. China
E-mail: wgcui@sjtu.edu.cn

The ORCID identification number(s) for the author(s) of this article can be found under https://doi.org/10.1002/adma.202207526.

Z. Kochovski, Y. Lu
Institute of Chemistry
University of Potsdam
14476 Potsdam, Germany

Z. Kochovski, Y. Lu
Institute of Electrochemical Energy Storage
Helmholtz-Zentrum Berlin für Materialien und Energie
14109 Berlin, Germany

P. Besenius
Department of Chemistry
Johannes Gutenberg University Mainz
Duesbergweg 10-14, 55128 Mainz, Germany

G. Chen
Multiscale Research Institute of Complex Systems
Fudan University
Shanghai 200433, P. R. China

DOI: 10.1002/adma.202207526

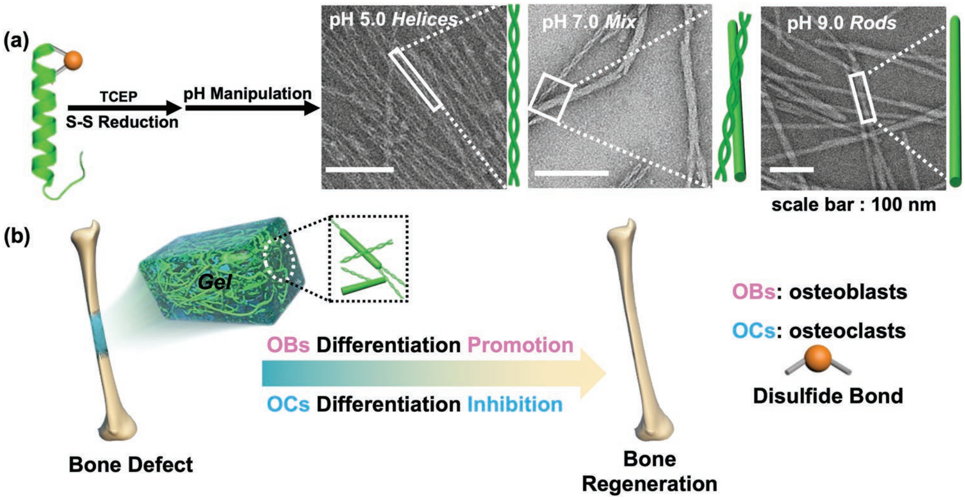

Scheme 1. a) Schematic diagram of the manipulation of sCT self-assembly and negative-stained TEM images of the assemblies (Helices, Mix, and Rods) at pH 5.0, 7.0, and 9.0. b) Schematic demonstration of sCT self-assembled hydrogel (Gel) enhancing bone regeneration for defected bone treatment.

field still lacks strategies to assemble bioactive proteins into regular structures at nano and micrometer scale with enhanced functionalities, that is, building "active protein materials" with functionality controlled mainly by their supramolecular structural features. The advantage of this type of materials is quite obvious: the active protein material contains active protein as both effective component and nanocarrier, which could significantly enhance the effective time scale of the protein, protect the active protein, and meanwhile decrease the side effect brought from other non-protein components.

Osteoporosis is mainly caused by an imbalance between bone-forming osteoblasts (OBs) and bone-resorbing osteoclasts (OCs), characterized by low bone mineral density (BMD), reduction in bone mass, and poor bone strength, leading to skeletal fragility and susceptibility to fractures.[13,14] The above features lead to bone fragility and it is highly challenging for bone healing under osteoporotic condition. Treatment with anti-osteoporosis drugs to promote bone formation or inhibiting OCs activity is one attractive strategy but with low efficiency, because of the insufficient drug concentration at the defective region due to the lack of blood circulation in the early stages of trauma.[15] To solve this problem, filling bone defects with some bioactive scaffolds have been investigated. However, the utilized materials like calcium phosphate cement, hydroxyapatite, and tricalcium phosphate are lacking osteoinductivity, making them difficult to achieve high therapy efficiency.[16,17] Thus it is urgent to develop a novel materials' construction strategy for osteoporosis bone defects therapy, which requires high biocompatibility, drug-loading efficiency, and versatility. Herein, we propose the concept of active protein materials, and intend to prepare such materials by using effective manipulation on the assembly morphology and packing pattern of the protein drug. Within this material, there will be only the active protein component with a scant amount of small-molecular "regulator." The protein material could show much higher biological activity than the protein itself in the monomeric state not only in vitro, but also in vivo applications. To this goal, salmon calcitonin (sCT) will be introduced as the protein component, which has been applied as a therapeutic agent for metabolic bone disease for more than 30 years.[18] The role of sCT is to reduce blood calcium (Ca^{2+}) and resist the action of parathyroid hormone.[19,20] Although sCT has been approved for the treatment of postmenopausal osteoporosis, bone related pain of Paget's disease, and hypercalcemia in several countries,[21] the property of sCT requires the drug to be made into lyophilized powder for injection treatment, mainly due to its instability and short half-time. Thus, there is still plenty of room to improve the formulation of sCT for high bioavailability and long circulation time, in order to minimize the need for repeated administrations. In this paper, we will demonstrate that by careful modulation on the dynamic bond and PPIs that sCT participates, the morphology and packing pattern of sCT can be effectively manipulated, resulting in novel active protein material based on sCT, with an accelerated and significantly improved bone integration for defect even with osteoporosis compared to commercial formula of the protein drug itself (**Scheme 1**).

2. Results and Discussion

2.1. Choice of sCT and its Self-Assembled Morphologies

sCT is a polypeptide hormone comprised of 32 amino acids with a molecular weight of 3431.88 Da, which is secreted by the C cells of the thyroid in mammals and the ultimobranchial glands in submammals.[22] The native sCT is characterized by a primary sequence with a disulfide bond between the first and seventh cysteine (Scheme 1a, the disulfide bond represented as the orange ball), which is essential for secondary structure formation and retention of sCT.[23] The unique character in structure provides opportunity to improve the pharmacological activity by regulating the aggregation state of sCT. It is well known that the disulfide bond is a dynamic covalent bond and has been widely applied in drug delivery systems, biomaterials fabrication, and dynamic material construction, because of its controllable reversibility.[24–26] Thus, the existence of disulfide bridge in sCT sequence inspires us to take it as the "target" for manipulating and modulating the assembly process of sCT by reversible formation of the disulfide bond to construct more effective active biomaterials than virgin sCT. Furthermore, the exchange reaction of the thiol–disulfide system is water compatible, relatively fast, and the kinetics can easily be controlled by the oxidation–reduction state of the thiol group. Tris(2-carboxyethyl)phosphine (TCEP) is an efficient reducing agent for disulfide bonds and has been widely used in biochemistry because of the high reaction specificity and water solubility.[27] Meanwhile, the oxidation rate of TCEP is closely related to pH value in a wide range of the microenvironment as follows: the oxidation rate is pretty slow in acidic conditions, and it takes more than 24 h to oxidize 10% of TCEP at pH 5.0. However, more than 70% of TCEP will be oxidized after 24 h at pH 7.4, losing its capacity to act as reducing agent. When pH reaches 11.6, TCEP will be oxidized quickly and totally (Figure S1, Supporting Information).[28] The high sensitivity of TCEP to pH makes it possible to regulate the state of sulfhydryl groups effectively by just slightly adjusting the pH of its environment. Thus, in this study, TCEP was employed to perform as the regulator of thiol–disulfide formation for sCT assemblies' construction with different microstructures. Although the pH condition might generally change the aggregation state of proteins, fortunately sCT has an isoelectric point (pI) of 10.4 guaranteeing its existence as a dissociative cation but not leading to sedimentation at a pH below 10.4, which is another reason for choosing sCT as the model protein building active protein materials.[29] The above features of sCT and TCEP encourage us to control the disulfide bond formation kinetics via pH with the minimized effect on the aggregation behavior of sCT.

Thus in this work, sCT was incubated with TCEP to reduce disulfide bond first and induce self-assembly under different pH to construct precise microscale morphologies. Briefly, equimolar TCEP solution was added to sCT followed with incubation for 30 min. HPLC was employed to detect the reduction efficiency showing the opening efficiency of the disulfide bonds (Figure S2, Supporting Information). Then buffers with pH 5.0, 7.0, and 9.0 were chosen to manipulate the redox state of the thiol groups. Briefly, 0.5 mL buffer was added to 0.5 mL reduced sCT (2 mg mL^{-1}), ensuring the final concentration of sCT was 1 mg mL^{-1}, which was then stirred at room temperature. After 30 min, the solutions all showed Tyndall Effect, suggesting the aggregation of the reduced sCT monomer. Even 12 h later, all the protein solution was clear with strong Tyndall Effect and no precipitates were observed. TEM was employed to investigate the microstructures of the self-assemblies under these conditions. As shown in Scheme 1a, at pH 5.0, double helices ("Helices," for clarity) were captured with an average width of 10 nm. When pH was increased to 9.0, nanorods ("Rods," for clarity) with the diameter of 15 nm were observed. Both the Helices and Rods and bundled Rods existed under the condition of pH 7.0 ("Mix"). It is worth mentioning that, the Helices and Rods were the dominant morphologies at pH 5.0 and 9.0, respectively, which was supported by TEM images at large scale (Figure S3a,b, Supporting Information).

2.2. The Mechanism for Helices and Rods Formation of Reduced sCT Monomer

Such different morphologies of Helices and Rods of reduced sCT monomer at pH 5.0 and 9.0, respectively, inspired our great interest to study the assembly mechanism in detail. To explore the self-assembly process of reduced sCT monomer under different conditions, the dynamics of sCT assembly were monitored by circular dichroism (CD) to investigate the secondary structure changes upon time, and dynamic light scattering (DLS) was employed to monitor the scattered light intensity ($<I_s>/<I_0>$) of the aggregated states. Under the condition of pH 5.0, the CD spectrum was monitored for 120 h and found that the signal strength at $\lambda = 195$ nm increased and the signal at $\lambda = 222$ nm decreased rapidly over time (Figure S4a, Supporting Information), which suggested the quick formation of β-sheet structure in the self-assembly process. By following the signal at $\lambda = 195$ nm in time, a rapid increase was observed after about 7 h (**Figure 1**a, the black line). According to the DLS results, in the first 2 h, $<I_s>/<I_0>$ showed a dramatic increase, which demonstrated the rapid aggregation of the reduced sCT monomer in the initial stage. Then the increase rate of $<I_s>/<I_0>$ gradually slowed down and reached a plateau after 14 h (Figure 1a, orange line). From the CD spectra and DLS results upon time, one may find that during the whole evolution time, the change of sCT aggregation stage was accompanied by an increase in the β-sheet signal. Meanwhile, time-dependent TEM was carried out to capture the nanoscale morphologies at every stage of the self-assembly process (Figure 1b–d). As the TEM micrographs showed, spheres were found at the first 5 min of incubation, with an average diameter of 23 nm and strong fusion tendency. Over the next 15 min, the spherical assemblies would connect with each other and further stack into short nanofibers. The rapid formation and fusion of the basic aggregates was consistent with the fast growth of $<I_s>/<I_0>$ at initial stage, mainly driven by the β-sheet formation, as observed in CD spectroscopy. These originally formed β-sheet structures were further found to rearrange into long double helix structures and finally gave the Helices with an average width of 10 nm within 12 h. The double helix structure of Helices was further confirmed by reference-free 2D class averaging (details shown in Figure S3c, Supporting Information), showing a clear double helix feature (Figure 1e). The TEM results explained the second stage of DLS quite well. The fusion of spheres into short nanofibers was supported by the increase of $<I_s>/<I_0>$, then the rearrangement to double helix retarded the increase, while the rearrangement stage from the original spheres with β-sheet structures to Helices was accompanied by the constant increase of CD signal, indicating the increased formation of regular β-sheet structures during the process.

The same monitoring operation was performed under the assembly conditions at pH 9.0. CD spectra (Figure S4b, Supporting Information) showed the similar change tendency to the trend shown in Figure S4a, Supporting Information, with an increase of the β-sheet signal at $\lambda = 195$ nm. However, when the time-dependent characteristic signal variation at $\lambda = 195$ nm (as that in Figure 1a) was plotted in Figure 1f, the increase of the signal intensity at pH 9.0 was quite different from that in

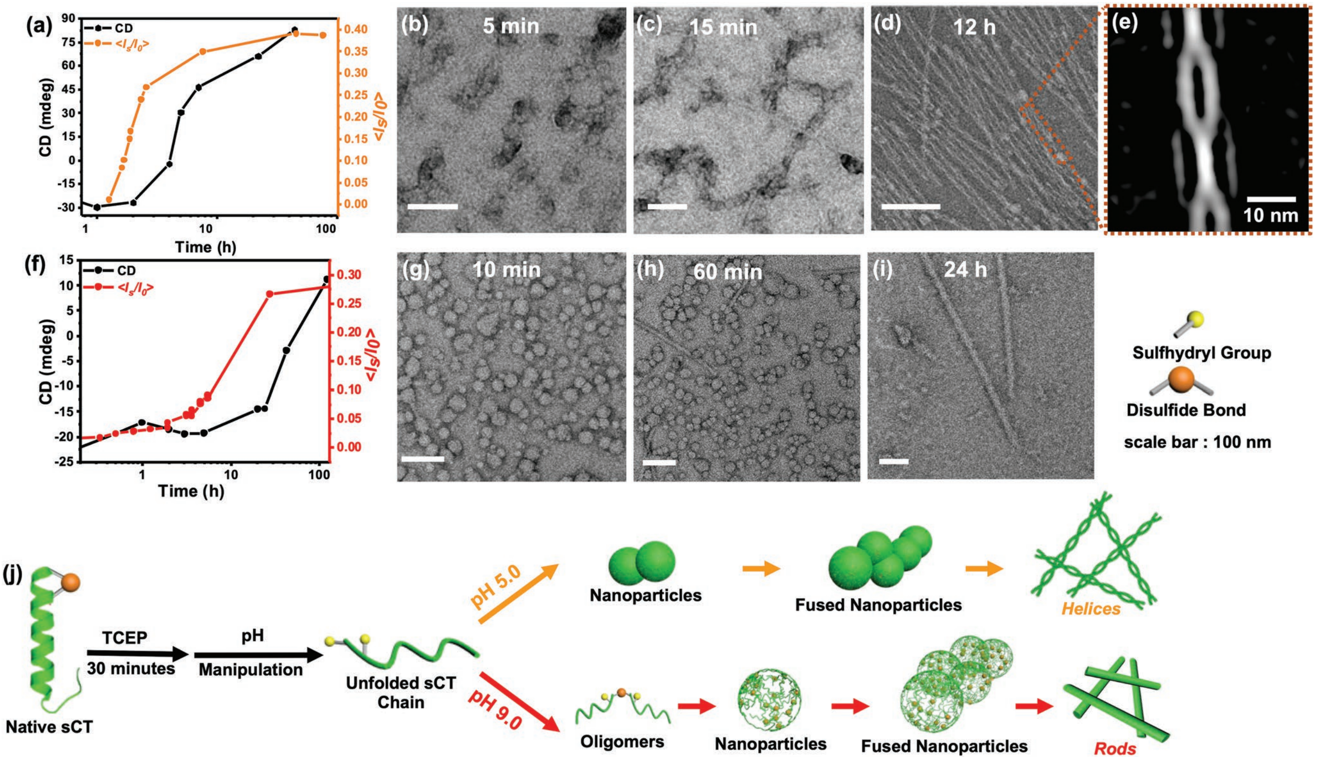

Figure 1. a) Graph showing the intensities of the CD band at $\lambda = 195$ nm (black line) and $<I_s>/<I_0>$ (orange line) values change upon time at pH 5.0. b–d) Time-dependent negative-stain TEM images of reduced sCT monomer self-assembly process at pH 5.0: b) 5 min; c) 15 min; d) 12 h. e) 2D class average of boxed segments from Cryo-EM images of Helices. f) Graph showing the intensities of the CD band at $\lambda = 195$ nm (black line) and $<I_s>/<I_0>$ (red line) values change upon time at pH 9.0. g–i) Time-dependent negative-stain TEM images of reduced sCT self-assembly process at pH 9.0: g) 10 min; h) 60 min; i) 24 h. j) Schematic diagram of self-assembly mechanism of reduced sCT monomer at pH 5.0 (the upper one) and pH 9.0 (the bottom one) (scale bar 100 nm in TEM images and 10 nm for 2D class average [e]).

Figure 1a. The signal variation at $\lambda = 195$ nm upon time showed an obvious lag phase in the first 10 h (Figure 1f, black line), suggesting the weaker tendency to aggregate into β-sheets, compared with that under acidic condition. This phenomenon was further supported by other observations. First, it took nearly 42 h to present the typical β-sheet structure as strong as that in Figure S4a, Supporting Information (Figure S4b, Supporting Information). Furthermore, $<I_s>/<I_0>$ at pH 9.0 also showed a similar lag phase in the first 2 h to that of CD spectrum, instead of the rapid increase of $<I_s>/<I_0>$ in the case of Helices formation. After 10 h, $<I_s>/<I_0>$ rose over a short course of 1 h, and reached a plateau after 24 h (Figure 1f, red line). TEM captured spherical particles with a diameter about 20–40 nm in the first 10 min (Figure 1g). However, these spheres showed much larger size under TEM than that measured by DLS. It is generally known that the hydrodynamic radius $\langle R_h \rangle$ from DLS is larger than the size measured from TEM due to the solvation of the hydrophilic shell.[30,31] Thus AFM was further carried out for the height measurement of the spheres, indicating the spheres were just about 1.5 nm in height, which was much smaller than the diameter measured by TEM (Figure S5, Supporting Information). This phenomenon indicated that the spheres were quite loose ones, demonstrated by the very low apparent height under the force of the cantilever. This loose property was consistent with the previous measured diameter inconsistency via DLS and TEM. Thus, the obtained loose particles were quite different from the micelles observed at pH 5.0. Combining the lag phase observed from DLS and CD, it was speculated that the reduced sCT monomer aggregated through different pathway in the initial stage of Helices and Rods formation. As time increased, the loose spheres were observed to be aligned to nanorods, which became dominant under microscopy after 24 h.

From the above results, one may find that, the slight difference of self-assembly condition led to such dramatic differences in dynamic process and morphology change. In this process, there are mainly two driving forces for self-assembly of the reduced sCT monomer including PPIs and disulfide bond reconstruction. The chosen pH values were all below the pI of sCT, which suggests the minimal differences in the PPIs when varying the pH value. In contrast, the sensitivity of TCEP oxidation to pH has an influence on the oxidation rate of the sulfhydryl groups, which might be the most obvious and decisive factor. After TCEP reduction, the intra-molecular disulfide bridges were open and the remaining thiol groups were susceptible to be oxidized by oxygen. The side reaction of TCEP oxidation is much slower under acidic conditions than the alkaline conditions.[28] Thus the different amount of sulfhydryl groups under different conditions may participate in the nanostructure reconstruction and affect the morphology transition kinetics significantly. In the Helices formation process (pH 5.0), there might exist large amount of dissociative sulfhydryl groups and it was difficult for disulfide bonds reconstruction (Figure 1j, upper one). While, the PPIs between the reduced sCT should be the main driving force to induce the aggregation of proteins to form spheres first. CD spectra confirmed the quick construction of β-sheet structures. Then with time going by, the reconstruction of disulfide bonds facilitated the micelle fusion and rearrangement of protein aggregates into Helices. On the contrary, TCEP would be oxidized more rapidly under alkaline condition, which sped up the formation of disulfide bridges and the oligomerization of the reduced sCT. As an important evidence of disulfide bond formation, sCT dimer has been captured by MALDI-TOF MS at the initial stage when pH was 9.0, while it was hard to be observed under acidic condition (Figure S6, Supporting Information) after self-assembly for 1 h. The lag phase observed from DLS was quite different from that of Helices formation, which could be explained as the dimerization-dominant stage of sCT under pH 9.0. Then the aggregation driven by PPIs brought the dimers to loose particles and finally Rods. We supposed that the major reason for loose micelle formation came from the dimerization or oligomerization of reduced sCT monomer, which made the proteins aggregate incompactly (Figure 1j, the bottom one). From the above results and discussion, one may find that there is a subtle trade-off between the dimerization of sCT via disulfide bond formation and the aggregation of sCT induced by PPIs (Figure 1j). With just slight change on the kinetics of disulfide bond formation, the self-assembly kinetics could be manipulated, resulting in different assembly pathways and different morphologies.

To further confirm the critical role of disulfide bond formation in the morphology control of sCT assembly, the reduced sCT monomer was modified by mPEG-acrylate through thiol–ene click reaction at different condition.[32] It was assumed that block of the free sulfhydryl groups could prevent the morphology transition, if the disulfide bond contributes significantly to the process. Typically, excessive mPEG-acrylate was added into the reduced sCT solution for quick reaction, when the self-assembly process was still at an early stage. Under the condition of Helices formation, where the disulfide bonds formation was supposed to be retarded, PEGylation began 60 min later after reduction, when the CD signal did not show strong characteristic peaks of β-sheets. It was found that the CD signal remained the same as that before the addition of mPEG-acrylate and showed no increase at $\lambda = 195$ nm or decrease at $\lambda = 222$ nm (Figure S7a, Supporting Information). It demonstrated that the addition of mPEG-acrylate successfully prevented the further assembly of sCT and froze the assembly of sCT at the state when mPEG-acrylate was added. TEM results showed there were already some Helices structures formed at 60 min (Figure S7b,c, Supporting Information). With the passage of time, although the signal of CD continued to change, the morphology was basically determined. The results proved PPIs drove the self-assembly process mainly. Under pH 9.0, because of the low self-assembly speed, the time interval of 180 min was selected. After the addition of mPEG-acrylate, the state remained at 180 min (Figure S7d, Supporting Information). TEM images demonstrated that after modification, only spherical morphology was observed even after 120 h (Figure S7e,f, Supporting Information). It was because of the blocking of sulfhydryl groups, preventing the further aggregation of reduced sCT.

2.3. The Self-Assembly of Reduced sCT Monomer at pH 7 and Hydrogel (Gel) Formation

Based on the above-discussed mechanism and the results of Helices and Rods, we were curious to tune the balance of disulfide bonds formation and PPIs to afford relatively cross-linked samples as biocompatible materials. Considering the oxidation speed of TCEP at pH 7.0 is between those of 5.0 and 9.0, it was expected that at pH 7.0 the disulfide bonds formation and PPIs could contribute concordantly, which means that the morphologies of Helices and Rods may randomly exist together, generating cross-linked networks. Thus, sCT was reduced following the previous procedures with addition of buffer (pH 7.0). After 12 h, the mixture of Helices and Rods was observed by TEM at the same time. CD was also carried out but showed different trend from those of pH 5.0 and 9.0, that is, the signal strength at 197 nm increased from −25 to −5 medg within 30 min and stayed stable till 120 h (Figure S8, Supporting Information). As shown in **Figure 2**a, the plotted CD signal at 195 nm with time showed a rapid increase trend at the initial state, which was similar to the trend that observed in the case of pH 5.0. $\langle I_s\rangle/\langle I_0\rangle$ results showed a retarded increase in the self-assembly process, which was similar to that at pH 9.0. Time-dependent TEM observed nanoparticles with the diameter of 40–60 nm in the first 10 min. After 30 min, short Helices and Rods were captured at the same time. Nearly 12 h later, there existed long Helices and Rods and bundling of two Helices (Figure 2b–d). The assembly behavior of sCT at pH 7.0 indicated that this condition has the potential for functional protein hydrogel fabrication.

As expected, protein hydrogel (Gel, for clarity) formed rapidly only at pH 7.0 (Figure 2e) when the concentration was risen to 20 mg mL^{-1}. On the contrary, there was just “thick” protein solution generated at pH 5.0 and 9.0 (Figure 2e). This result indicated that tuning the equilibrium between disulfide bonds reconstruction rate and PPIs increased the possibilities of intermolecular cross-linking. The bundled Rods may be the cross-linking point for Gel formation according to the TEM image shown in Figure 2d. Rheological behavior of Gel was measured with a rheometer. In the experimental range, the storage (G') modulus of protein hydrogel formed under pH 7.0 were much larger than the loss (G'') modulus (Figure 2f), indicating that the protein assemblies exhibited characteristic feature of hydrogel. The network formed in Gel may improve the stability of sCT and protect sCT from fast degradation, which showed the potential to improve the ability of bone regeneration. To this goal, the release of Gel and virgin sCT was detected by transferring them into dialysis bags (molecular-weight cutoff (MWCO) 100 kDa), respectively, in PBS with 10×10^{-3} M DTT at 37 °C and the cumulative amount of sCT with time was assessed by the Bradford method. After mild shaking for 30 h, virgin sCT was released into PBS totally, while the release rate of sCT was observed to be much slower from the network of Gel and only about 60% of sCT was released in the end (Figure 2g). To further demonstrate the release profile of Gel, taking the widely used polyethylene glycol diacrylate (PEGDA) gel as a control scaffold with the same amount of sCT-loaded (PEGDA gel for short, preparation detail in Experimental Section), the release rate of sCT from Gel was similar to that from PEGDA gel. It

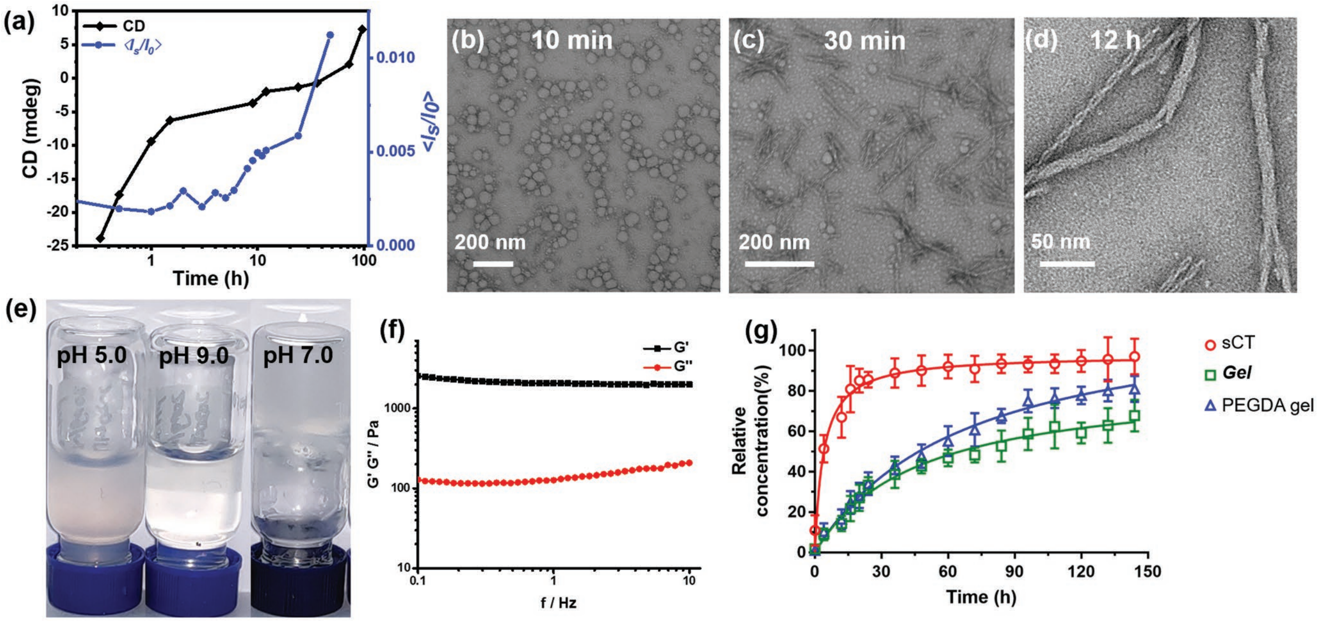

Figure 2. a) Graph of CD spectrum at 195 nm (black line) and $<I_s>/<I_0>$ (blue line) values changes with time at pH 7.0. b–d) Time-dependent negative-stain TEM images of reduced sCT self-assembly process at pH 7.0: b) 10 min; c) 30 min; d) 12 h. e) Images of sCT assemblies solution at the concentration of 20 mg mL^{-1} at pH 5.0, 7.0, and 9.0. f) Frequency-dependent storage modulus (G') and loss modulus (G'') of Gel formed under pH 7.0. g) Cumulative release of virgin sCT, Gel, and PEGDA gel in PBS with 10×10^{-3} M dithiothreitol (DTT) at 37 °C.

proved that disulfide bonds and cross-linked network of generated Gel retarded the release and degradation of sCT, which provided one alternative method to improve the half-time of sCT for its biomedical application.

2.4. Biocompatibility of sCT Assemblies

With the above Helices, Rods, and Gel in hand, their ability to perform the functionality of sCT became the important issue in the design and preparation of active protein materials. Although only very limited amount of TCEP was employed in the solution of sCT, the biocompatibility of the resulting active protein materials still needed to be proved. The proliferation and viability of stimulated bone marrow stromal cells (BMSCs) was tested after incubation with different sCT assemblies for 1, 3, and 5 days. Cells survived well at different time points in all groups showed by the Live/Dead staining, and the dead cells were almost invisible (Figure S9, Supporting Information). Furthermore, Cell Counting Kit-8 (CCK-8) assay also demonstrated good proliferation of BMSCs and fine viability in each group within the extended culture time (Figure S10, Supporting Information). Combining the abovementioned two main assays, all of the Helices, Rods, and Gel of sCT possessed good biocompatibility.

2.5. Gel Regulates the Expression of Osteogenic Differentiation-Related Genes

To investigate the effect of different sCT assemblies on the expression of osteogenic differentiation-related genes in BMSCs, corresponding cells were incubated with PBS (positive control), virgin sCT, and sCT assemblies (including Helices, Rods, Gel, with the same amount of sCT) in OIC media for 10 days, while the control group was incubated in normal media (negative control). It was found that, alkaline phosphatase (ALP), runt-related transcription factor 2 (Runx2), collagen type 1 (Col1*α*), and Osteoprotegerin (OPG), were significantly upregulated in virgin sCT- and sCT assemblies-treated groups compared to those incubated in normal medium and the PBS groups. Very interestingly, the upregulation of these factors treated by Gel was much higher than those treated by virgin sCT and sCT assemblies (Helices and Rods). In detail, the mRNA fold changes in ALP, Runx2, Col1*α*, and OPG in Gel group than those in control groups were as much as 10.74, 3.19, 14.65, and 14.07, respectively (**Figure 3**a–d). Meanwhile, the expression of OC differentiation-related genes was detected in pre-OCs, which were incubated with PBS and the same concentration of virgin sCT and sCT assemblies (including Helices, Rods, and Gel) in *α*-modified Eagle's medium (*α*-MEM) media with receptor activator of nuclear factor kappa-B ligand (RANKL) for 4–5 days, and the control group was incubated without RANKL. Analogously, all the OC differentiation-related genes, including c-Fos, nuclear factor of activated T cells C (NFATC), cathepsin K (CTSK), and tartrate-resistant acid phosphatase (TRAP) were also dramatically downregulated after the treatment of Helics, Rods, and Gel than those in PBS group. Notably, all of the OC differentiation-related genes in Gel group were significantly lower than those in Helices and Rods groups (Figure 3e–h). The above results indicated that self-assembled sCT could improve the ability of the protein drug to promote osteogenic differentiation and inhibit OC differentiation at the genetic level, especially with the network in Gel.

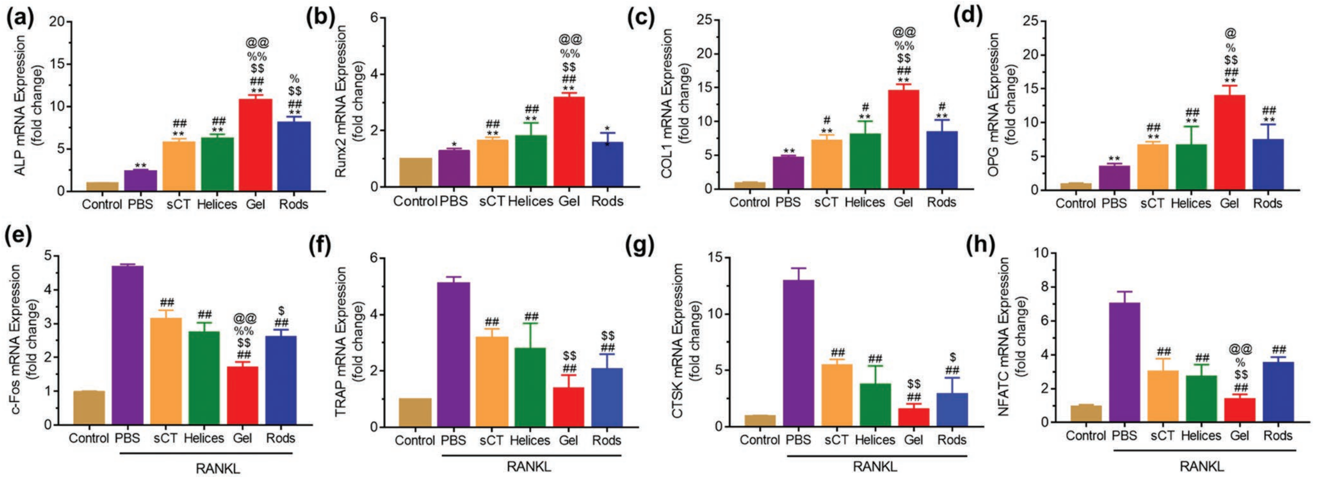

Figure 3. a–d) q-RT-PCR results of the expression of osteogenic differentiation-related genes in BMSCs including ALP mRNA (a), Runx2 mRNA (b), Col1α mRNA (c), and OPG mRNA (d); and e–h) osteoclast differentiation differentiation-related genes in pre-osteoclasts including c-Fos mRNA (e), TRAP mRNA (f), CTSK mRNA (g), and NFATC mRNA (h). Key: $^{**}p < 0.01$ (vs Control); $^{\#}p < 0.05$, $^{\#\#}p < 0.01$ (vs PBS); $^{\$\$}p < 0.01$ (vs sCT); $^{\%\%}p < 0.01$ (vs Helices); $^{@@}p < 0.01$ (vs Rods).

2.6. Gel Inhibits the Differentiation of Pre-Osteoclasts Cells and Bone-Mineralized Nodules

To address the direct effect of sCT assemblies, especially Gel on osteogenic differentiation, BMSCs incubated with sCT-related samples for 7 and 14 days were investigated by Alizarin Red (ARS) and ALP staining (details in Experimental Section). The stained mineral in the control group was increased slightly with the extended culture time, while the extent of ARS-stained bone-mineralized nodules in the Helices, Rods, and Gel groups was much more significant than that in the sCT group. Especially the Gel group appeared the highest amount of bone-mineralized nodules among all groups (**Figure** 4a,b). The calcium deposition spots in BMSCs treated with Gel were significantly larger than those in the other groups, which was more intuitive under the microscope (Figure S11a, Supporting Information). In addition, the ALP-staining and ALP-activity results were similar to the results of ARS-staining. Gel showed much better capability on osteogenic differentiation (Figure 4c,d). Furthermore, it is known that RANKL treatment induced the differentiation of pre-OC cells into OCs, which were represented by multinucleated TRAP cells.[33] When pre-OC cells were treated with RANKL in PBS, the large amount of TRAP-positive multinucleated OCs suggested the successful differentiation of pre-OC cells. However, when the cells were treated with both RANKL and virgin sCT or sCT assemblies, the number of TRAP-positive multinucleated OCs was significantly decreased, compared to the cells treated with PBS alone (Figure 4e). Interestingly, the number further decreased obviously in the Gel group. It was verified that sCT had the ability of suppressing OCs formation, suggesting that the Gel was superior to the virgin sCT in bone remolding.

2.7. Gel-Promoted Bone Integration in Osteoporosis

Based on the above results, Gel demonstrated the improved potential of bone regeneration ability. Therefore, rat distal femur defect model with osteoporosis was treated with virgin sCT, Gel, and PEGDA gel (the same sCT loaded as Gel did) for 12 weeks. To investigate the bone regeneration in the defected bone, X-ray, and micro-CT were employed to disclose the new bone formed in radiographic aspects. Meanwhile, the morphology and amount of new bone were quantitatively analyzed. As shown in **Figure 5**a, the drill defects in the control group were still almost hollow even at 12 weeks after the operations, while the model treated with Gel and PEGDA gel presented significantly higher percentage healing of defects, which were also much more effective than that treated by virgin sCT. The circular defect in the distal of femur was further reconstructed with the help of software and the newly formed bone was further evaluated. After treatment with Gel and PEGDA gel, BMD (Figure 5b) and bone volume/total volume (BV/TV) (Figure 5c) of the model, which reflected the recovery ability of the bone defect, were all significantly higher than those of the control group and the one treated by virgin sCT. The micro-CT results suggested that Gel and PEGDA gel had much better potential for bone integration than virgin sCT, and Gel demonstrated similar bone integration effect to PEGDA gel. Although compared with PEGDA gel, Gel group did not show much better bone regeneration ability, the simple component design of Gel has much higher atom economy than PEGDA gel, avoiding large amount of backbone polymer, which may bring loading efficiency and immunogenicity problems. These advantages make the active protein material design very promising compared to traditional method via drug-loading in polymeric hydrogels.

2.8. Gel Performs with a Notably Higher Osteogenic Capability in Degradation

In order to further evaluate the bone regeneration ability of Gel in vivo, histological staining experiments were employed. At 12 weeks of operation, the femurs samples were fixed and

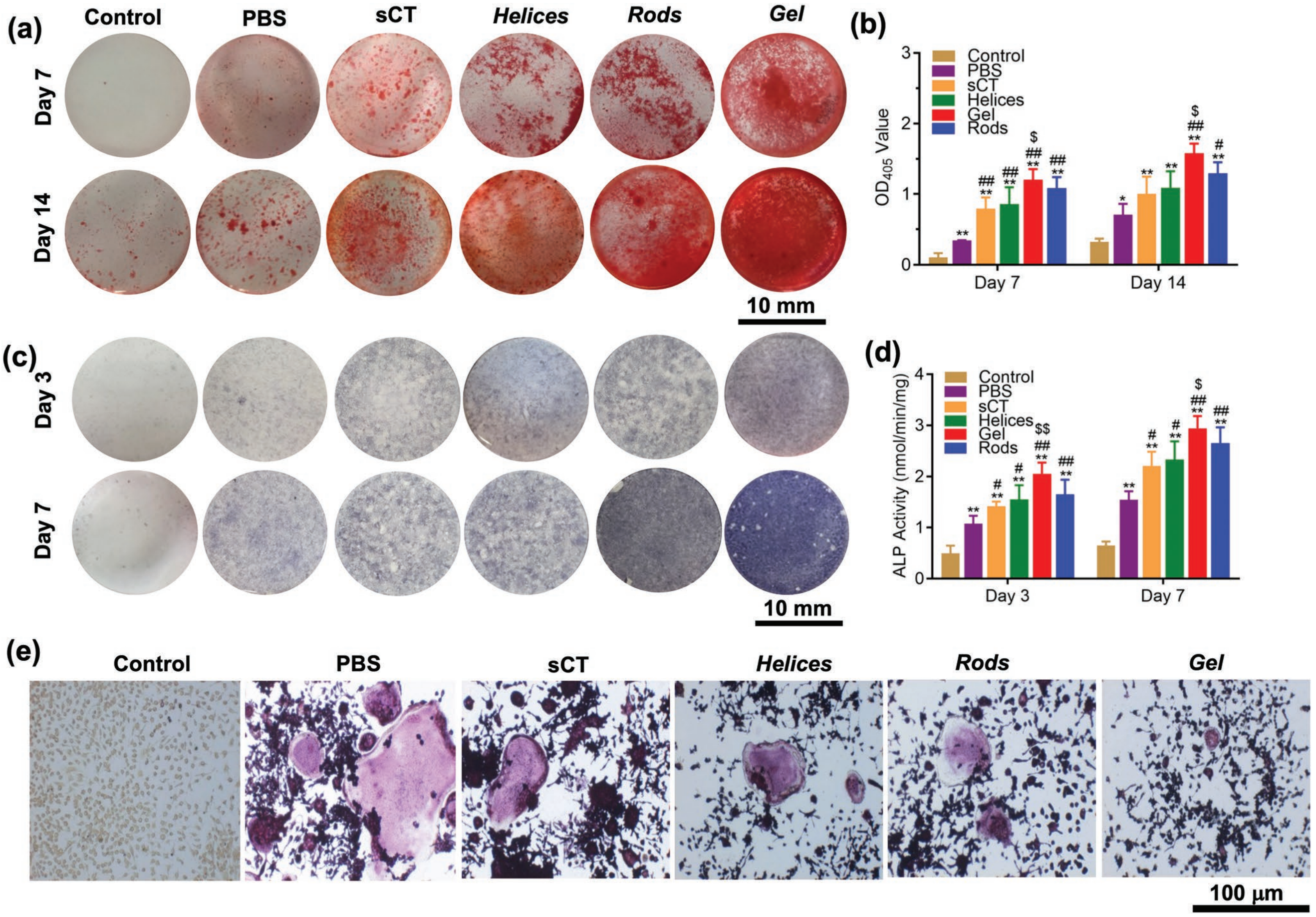

Figure 4. a,b) ARS staining for bone-mineralized nodules detection incubated for 7 and 14 days. The production of mineralized matrix was determined by quantifying the amount of Alizarin Red S that stained the mineralized matrix. The solution absorbance was measured at 405 nm with a microplate reader. c,d) ALP staining of bone-mineralized nodules detection incubated for 3 and 7 days. e) TRAP staining for osteoclasts formation in pre-osteoclasts cells after treatment of different samples. Scale Bar: 10 mm and 100 µm, respectively. Key: $**p < 0.01$ (vs Control); $^{\#}p < 0.05$, $^{\#\#}p < 0.01$ (vs PBS); $^{\$\$}p < 0.01$ (vs sCT); $^{\%\%}p < 0.01$ (vs Helices); $^{@@}p < 0.01$ (vs Rods).

decalcified, then representative hematoxylin–eosin (HE) staining sections were presented (**Figure 6**a). There showed no distinct inflammatory response or necrosis in all groups. More newly formed bone tissues (pointed by the yellow arrow), which spread from the margin to the center of the defect were detectable in experimental groups especially in the Gel and PEGDA gel groups than that in control group. Meanwhile, in the model treated by Gel and PEGDA gel, the defect channels were filled mostly, while only few newly formed bones appeared in the marginal defect region of the control group. Furthermore, immunohistochemical staining was carried out to evaluate the expression of Collagen type Iα (Col1α) in the bone tissue (Figure 6b,c). The brown areas indicated a positive expression of Col Iα (Figure 6b) in the new bone. After 12 weeks of repairing, control group exhibited a lower positive area than other groups, while new bone tissues were observed in abundance in experimental groups, especially in the Gel and PEGDA gel treated groups. Besides, the relative bone maturity value in the region of the defect in different groups at 12 weeks (Figure 6d) was measured. It suggested that the Gel and PEGDA gel have the better ability of promoting bone growth in the critical-size bone defect among the different groups. These results exhibited that the Gel and PEGDA gel groups had a notably higher osteogenic capability in rat distal femur defect model with osteoporosis compared with virgin sCT.

2.9. Gel Promotes Bone Integration for Bone Defect without Osteoporosis

The highly effective bone integration promotion of generated Gel encouraged us to apply it for bone defect therapy without osteoporosis. Therefore, rat distal femur defect model was treated with virgin sCT and Gel for 8 weeks. Similarly, the newly formed bone was detected by micro-CT and quantitatively analyzed. As expected, Gel presented significantly higher percentage healing of defects than that treated with virgin sCT while the drill defects in the control group were still almost hollow even at 8 weeks after the operations (**Figure 7**a). Besides, the BMD (Figure 7b), BV/TV (Figure 7c), and trabecular thickness (TB.TH) (Figure 7d) of the Gel-treated models were all significantly higher than those of the control group and the one treated by virgin sCT. While, the value of trabecular separation/spacing (TB.Sp) (Figure 7e), which stood for the mean width of

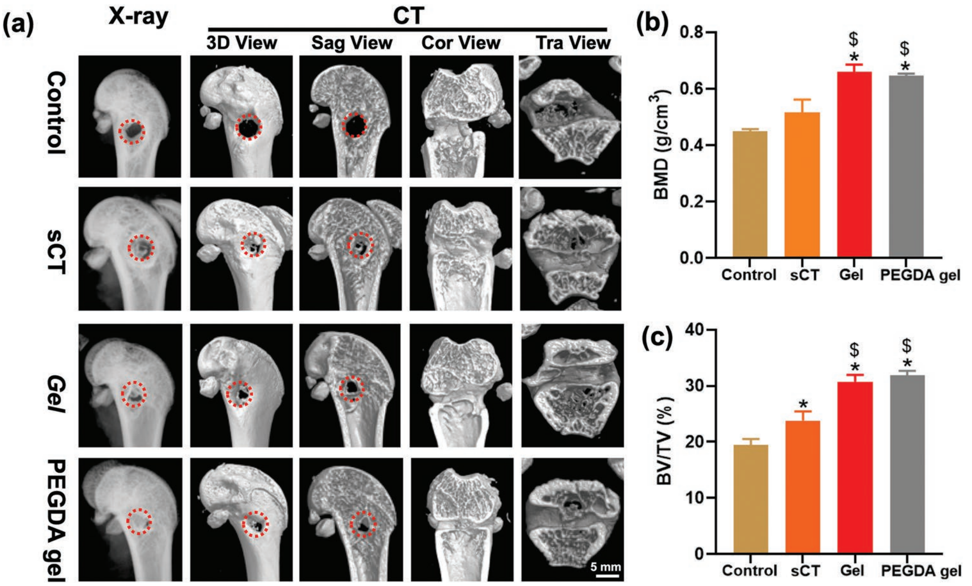

Figure 5. a) Micro-CT results of new bone formation in rat distal femur defect model with osteoporosis after the treatment of PBS, virgin sCT, Gel, and PEGDA gel. b,c) Recovery ability assessment results: b) BMD; c) BV/TV; scale bar: 5 mm. Key: $^*p < 0.05$ (vs Control); $^\$p < 0.05$ (vs sCT).

the medullary cavity between the trabecular bone, showed the similar trend, suggesting the decrease of bone resorption. All the obtained results in bone defect models without osteoporosis are consistent to those in bone defect with osteoporosis.

2.10. Gel Performs with a Notably Higher Osteogenic Capability for Bone Defects without Osteoporosis

Furthermore, histological staining experiments were employed in rat distal femur defect model by treating with virgin sCT and Gel for 8 weeks. First, representative HE staining sections were presented (**Figure 8**a). There showed no distinct inflammatory response or necrosis in all groups. Similar results with Section 2.7 were obtained. In detail, more newly formed bone tissues (pointed by the yellow arrow) were observed in Gel group than in control group. Meanwhile, in the model treated by Gel, the defect channels were filled mostly, while only few newly formed bones appeared in the marginal defect region of the control group. Second, the Masson staining also pointed to the similar results (Figure 8b) and the relative bone maturity value in the region of the defect in different groups were qualified at 8 weeks (Figure 8d). Furthermore, immunohistochemical staining was carried out to evaluate the expression of Col 1α in the bone tissue (Figure 8c,e), showing that abundant bone tissues were observed in experimental groups, especially in the Gel group.

The above results inspired us to explain the mechanism of the better bone regeneration capability of Gel than virgin sCT. When the bone was defected in osteoporosis, the microenvironment of OBs and OCs would change and then the balance between them was broken to some extent. Although bone resorption by OCs and bone regeneration by OBs both play key roles in bone tissue, for regeneration of new bones, more bone-forming than bone-resorbing, or more oOBs than OCs are expected. It is known that CT acts on OBs and OCs, and functions through limiting the number of OCs and inhibiting their motility and secretory activity, by inducing a burst of proliferation and functional activation of OBs.[34] The biological activities of CT are mediated by its binding to a specific receptor, the CT receptor (CTR), which belongs to the family of seven-transmembrane-domain G-protein-coupled receptors (GPCRs). It was found that CTR, like other GPCRs form homodimers and/or heterodimers, may alter the following signal transduction pathway and promote the function of CT. We speculate that, the sCT assemblies may promote dimerization and/or oligomerization of CTR via multivalent interactions, as the neighboring sCT in assemblies could bind with multiple CTR together, resulting enhanced biological activities (Figure 8f). However, there is still a long journey to investigate the detailed mechanism due to the complex microenvironment in vivo. Meanwhile, the slow release profile shown in Figure 2g indicates enhanced bioactivity of Gel than virgin sCT, which also contributes to the final improved bone repair results. The above results indicated that the developed strategy of single-component active protein materials by self-assembly manipulation in this work could be a practical method to enhance the biocompatibility and therapy efficiency of protein drug, compared to the traditional loading-and-release strategy in hydrogel.

3. Conclusion

We have developed a new strategy as bioactive materials construction for bone regeneration by manipulating the self-assembly of active monomer sCT. The dynamics and reversibility of disulfide bonds were utilized to control the self-assembly pathway. The assembled sCT materials, especially the Gel was proved to have much better capability for bone regeneration than virgin sCT, which may be explained by the slow release

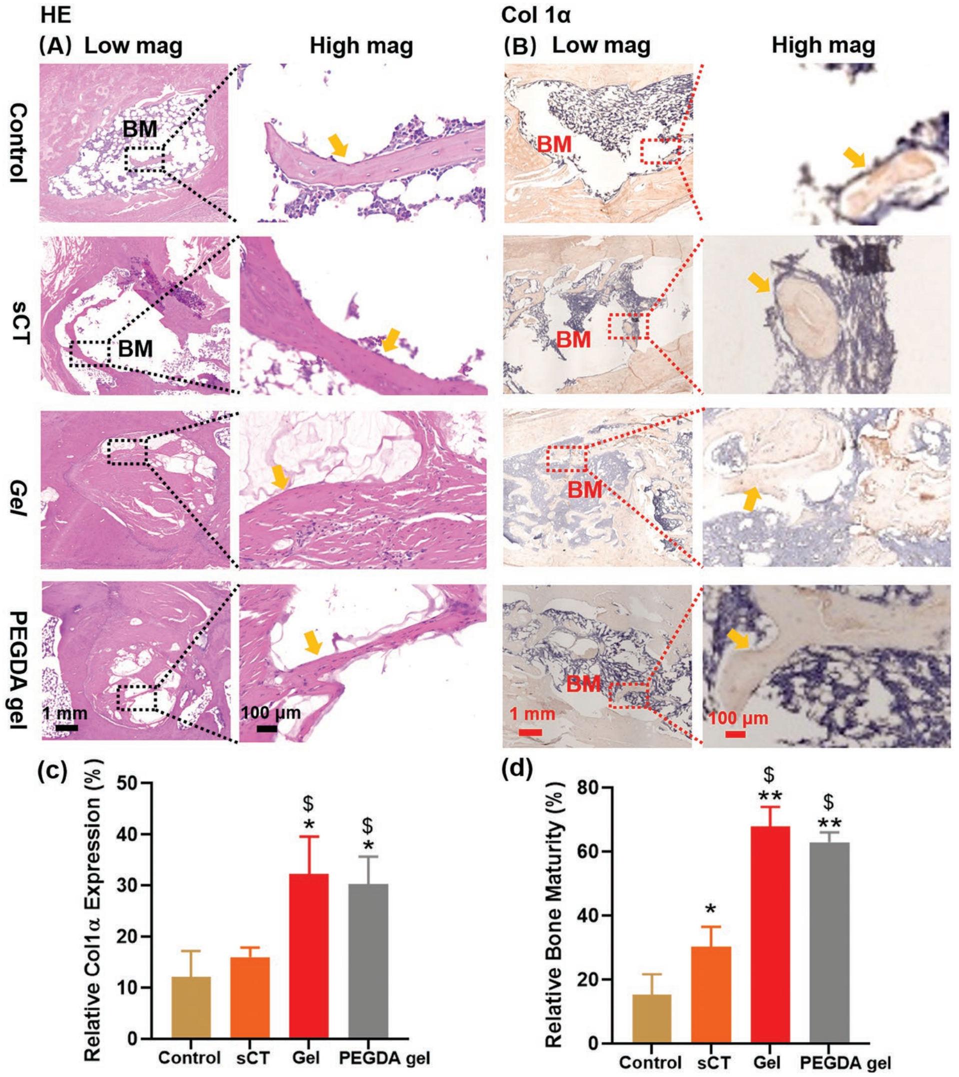

Figure 6. a) Representative HE staining. b) Representative immunohistochemical images of Col 1α staining of the harvested regenerated bone tissue at 12 weeks. c) The relative Col 1α expression in different groups at 12 weeks. d) The relative bone maturity value in different groups at 12 weeks Key: $^{**}p < 0.01$, $^{*}p < 0.05$ (vs Control); $^{\$\$}p < 0.01$, $^{\$}p < 0.05$ (vs sCT).

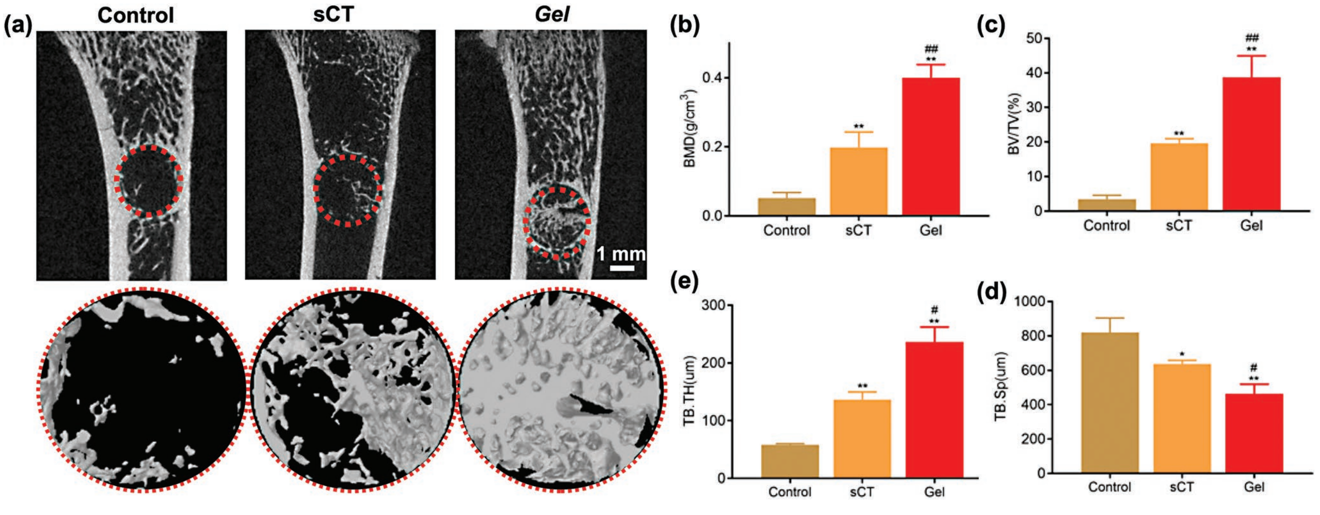

Figure 7. a) Micro-CT results for new bone formation with the treatment of sCT and Gel. b–d) Recovery ability assessment results: b) BMD; c) BV/TV; d) TB.TH; e) TB.Sp. Scale bar: 1 mm. Key: $^{**}p < 0.01$, $^{*}p < 0.05$ (vs Control); $^{\#\#}p < 0.01$, $^{\#}p < 0.05$ (vs sCT).

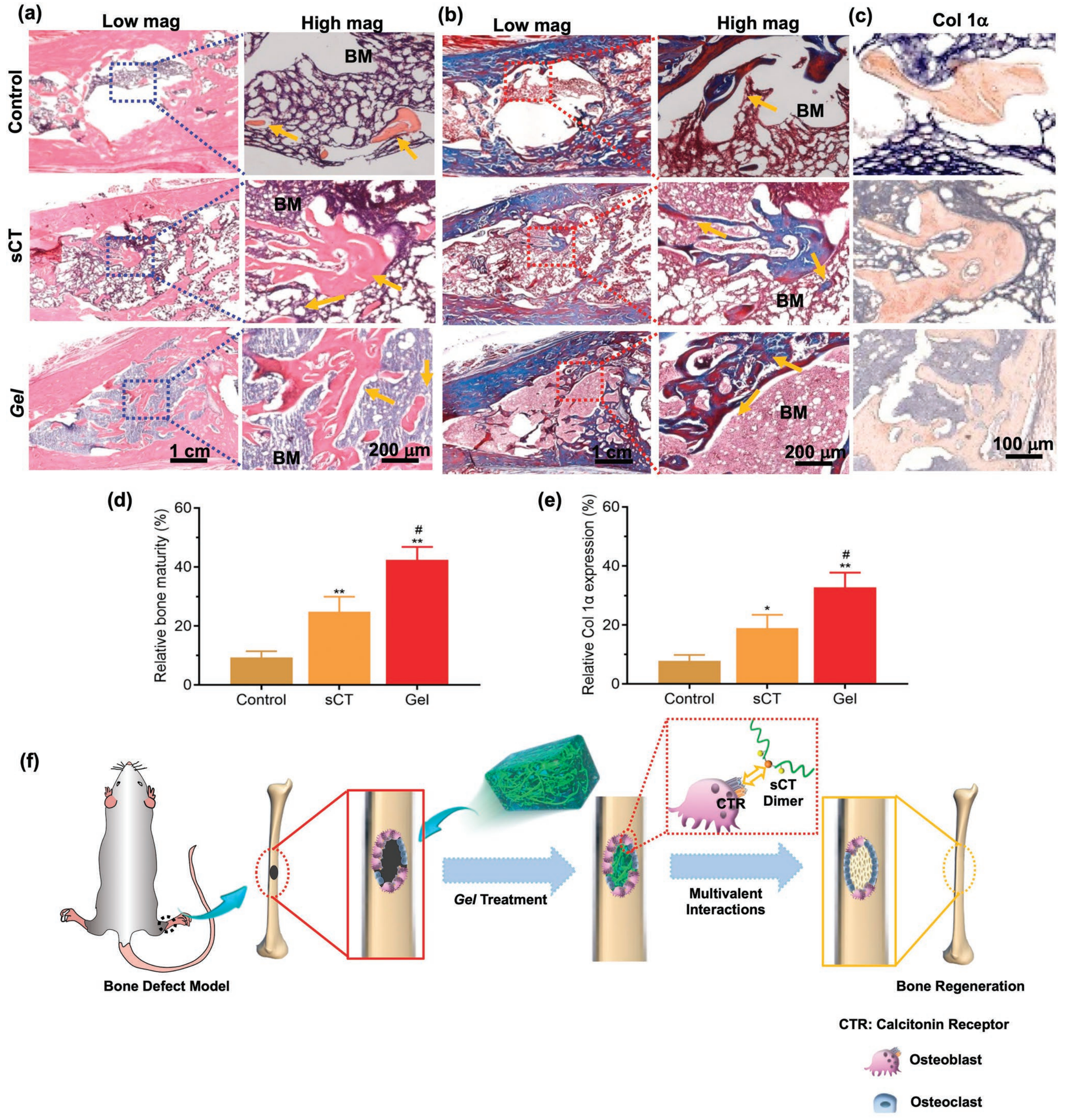

Figure 8. a) Representative HE staining and b) Masson staining and with different group treatment for 8 weeks. c) Representative immunohistochemical images of Col 1α staining of the harvested regenerated bone tissue at 8 weeks. d) The relative bone maturity value in different groups at 8 weeks. e) The relative Col1α expression in different groups at 8 weeks. f) Schematic presentation of the proposed mechanism of Gel-promoted bone regeneration. Key: $^{**}p < 0.01$, $^{*}p < 0.05$ (vs Control); $^{\#\#}p < 0.01$, $^{\#}p < 0.05$ (vs sCT).

profile of the Gel and multivalent binding of sCT assemblies to CTR. By using this active protein material construction strategy, sCT could be transformed to effective hydrogel as the drug and the carrier, which can be effectively manipulated from the viewpoints of protein self-assembly. The enhanced binding to receptors via multivalent effect, the slow release profile, high loading efficiency, and decreased degradation of the active protein drug all together indicate a bright future of this active protein material design. We believe that this simple and straightforward method may pave an alternative pathway for preparation of protein-related biomaterials with great potential in clinical applications.

4. Experimental Section

Chemicals and Materials: Chemicals were purchased from J&K Chemical, TCI and sCT was purchased from Aladdin, and all were used without further purification. Unless specially mentioned, all other chemicals were used as received.

Reduction of Salmon Calcitonin: Tris(2-carboxyethyl)phosphine hydrochloride (TCEP·HCl) was taken as the reduction reagent. Generally, sCT (4 mg, 1.166 µmol) was dissolved in 1 mL Milli-Q water. TCEP·HCl (3.3 mg, 11.66 µmol) was dissolved in 1 mL Milli-Q water. Then 0.1 mL of TCEP·HCl (11.66 µmol mL^{-1}) (equivalent amount with sCT) was added into the sCT solution and another 0.9 mL water was added to generate reduced sCT solution at the concentration of 2 mg mL^{-1}. Then the solution was stirred at room temperature for 0.5 h. The reduced sCT was used for further reaction without purification. The reduced sCT solution (40 mg mL^{-1}) was also made by adding 0.1 mL TCEP·HCl solution (66.8 mg mL^{-1}/233.2 µmol mL^{-1}) into 1 mL sCT solution (80 mg mL^{-1}) and another 0.9 mL water was added following with mild shaking at room temperature for 0.5 h.

sCT Assemblies Construction: Helices: 0.5 mL pH 5.0 buffer solution was added into 0.5 mL reduced sCT solution (2 mg mL^{-1}) and made the final concentration of sCT to be 1 mg mL^{-1}. The protein solution was stirred under room temperature.

Rods: 0.5 mL pH 9.0 buffer solution was added into 0.5 mL reduced sCT solution (2 mg mL^{-1}) and made the final concentration of sCT to be 1 mg mL^{-1}. The protein solution was stirred under room temperature.

Mix: 0.5 mL pH 7.0 buffer solution was added into 0.5 mL reduced sCT solution (2 mg mL^{-1}) and made the final concentration to be 1 mg mL^{-1}. The protein solution was stirred under room temperature.

Gel: 0.5 mL pH 7.0 buffer solution was added into 0.5 mL reduced sCT solution (40 mg mL^{-1}, which followed the procedure of “Reduction of Salmon Calcitonin”) and made the final concentration of sCT to be 20 mg mL^{-1}. The protein solution was stirred under room temperature for 12 h.

Preparation of PEGylated sCT: Poly(ethylene glycol) methyl ether acrylate (mPEG-Acrylate) (10 eq.) were added to reduced sCT solution and stirred under room temperature. The reaction efficiency was detected by HPLC after 2 h.

PEGDA gel Preparation: PEGDA was dissolved in PBS (10% w/v), and Irgacure2959 as a photoinitiator (0.5% w/w) was added to the solution system. The mixed solution was exposed to a UV light source (λ = 365 nm, power intensity = 17 mW cm^{-2}) for 30 s. Then, sCT (20 mg mL^{-1}) was added into the pre-polymerization solution, and further exposed to UV light for 40 s.

Release Study of Virgin sCT, Gel, and PEGDA gel: 5 mL virgin sCT, Gel, and PEGDA gel (the concentration of sCT in the all samples was 20 mg mL^{-1}) was transferred into dialysis bags (MWCO 100 kDa) and put in 300 mL 1× PBS with 10×10^{-3} M DTT at 37°C under a mild shaking condition (50 rpm). 0.2 mL releasing solution was withdrawn from PBS periodically. The cumulative amount of sCT was assessed by Bradford method.

Cell Culture: Rat BMSCs were cultured in Dulbecco’s modified Eagle’s medium (DMEM, Gibco) containing 10% fetal bovine serum (FBS, Gibco) and 1% penicillin/streptomycin (Gibco) at 37 °C with 5% CO$_2$, while pre-OCs were isolated from the medullary cavity of the femur of newborn rats and cultured in α-MEM (Gibco, US) with 30 ng mL^{-1} M-CSF (Novoprotein) containing 10% FBS and 1% penicillin/streptomycin in the same conditions.

Biocompatibility Test: CCK-8 was employed to analyze the proliferation behavior of BMSCs after treating with 2 mg mL^{-1} sCT or the self-assembly analogues, which was performed according to the protocol provide by Dojindo company. In brief, the test reagent was mixed with fresh DMEM on day 1, 3, and 5 and incubated for 2 h at a constant incubator containing 5% CO$_2$. Then the mixed solution absorbance was quantified by a microplate reader (Infinite F50, TECAN) at 450 nm. Besides, Live/Dead cell kit (Invitrogen) was applied to assess the viability of BMSCs after treating with 2 mg mL^{-1} sCT or the self-assembly analogues. After incubation for same days, cells were labeled with 500 µL of prepared dye consisting for 30 min, and the fluorescence images were acquired by confocal laser scanning microscopy (LSCM, LSM800, ZEISS). According to the manufacturer’s protocol, green represented the viable cells stained by calcein AM, whereas red meant dead cells dyed by EthD-1.

Alizarin Red S (ARS) Staining: The density of initial seeded cells was 10 000 per well and they were cultured for 7 or 14 days treating with 1 mg mL^{-1} sCT or the self-assembly analogues, which were cultured with osteo-inductive medium (Cyagen Biosciences) and then assigned to ARS staining (Cyagen Biosciences), which was used to detect the calcium nodule during osteogenic differentiation and assess the degree of osteogenic differentiation in vitro. In short, each sample was washed with D-PBS, fixed with PFM, and stained with ARS solution for 30 min. After that, they were further arranged to wash with D-PBS for three times, and imaged by a digital camera. Cells were co-incubated with 10% acetic acid for overnight, and the supernatant was collected by centrifugation and neutralized with 10% ammonium hydroxide in order to quantify the value of ARS staining through measuring the absorbance of supernatant at 405 nm.

ALP Staining and Activity: The presence of ALP was visualized by staining following the protocol (ALP Color Development Kit, Beyotime). Briefly, BMSCs were cultured with osteo-inductive medium in the same way mentioned above. On day 3 and 7, they were fixed by PFM, washed with DPBS, and incubated with ALP staining for 30 min in dark. Ultimately, each well was washed again and the results were obtained by a digital camera. The ALP activity was measured by a kit (ALP Assay Kit, Beyotime) at 3 and 7 days, according to the manufacturer’s guidance.

Tartrate-Resistant Acid Phosphatase Staining: OCs were differentiated from pre-OCs via adding RANKL (100 ng mL^{-1}, Novoprotein) into α-MEM and treating with 2 mg mL^{-1} sCT or the self-assembly analogues for culturing for 4–5 days. During the culture cycle, medium was changed twice. TRAP assay kit (Beyotime) was employed to detect the positive OCs, according to the manufactures’ protocol. Mature OCs were deemed that the nuclei were more than three in TRAP-positive cells.

Quantitative Real-Time Polymerase Chain Reaction Assay: The gene expressions of several major markers of osteogenesis and OC related genes were further detected by quantitative real-time polymerase chain reaction. The primer sequences used are shown in Table S1, Supporting Information. The Trizol reagent (Invitrogen) was used to extract the total RNA and the complementary DNA was synthesized by a PrimeScript RT reagent Kit (TakaRa). The amplification of genes were detected by an ABI 7500 real-time polymerase chain reaction (PCR) System (Applied Biosystems) using a SYBR Green quantitative real-time-PCR kit (TakaRa).

Animal Experiments: The osteogenic ability of sCT, Gel, and PEGDA gel in vivo was investigated by the rat distal femur defect model in osteoporosis. All animal procedures were performed in accordance with the National Institutes of Health Guide for Care and approved by the Animal Care and Use Committee of Shanghai Ruijin Hospital (SYXK (Hu) 2018-0027). Totally, 24 ovariectomized osteoporotic rat models with 8 weeks old were established, and housed in standard pathogen-free cage with suitable temperature. First, after all rats were anesthetized, small incisions were made on both sides of the dorsal third lumbar vertebrae, followed by blunt dissection and location of the ovary. Second, the fallopian tube which was attached to the end was ligated and cut, and the remaining tissue was removed. Finally, the incision was sutured 3 months after the operation, the successful rat model of osteoporosis was established and verified. In order to investigate the osteogenic ability of sCT, Gel, and PEGDA gel in vivo, four groups were randomly divided: un-treated group, sCT-treated group, Gel-group, and PEGDA gel group. Briefly, intraperitoneal anesthesia of pentobarbital sodium (30 mg kg^{-1}) was applied to the experimental rats and then a distal femoral thigh incision was made for exposing femoral condyle. An electric hand drill equipped with a diameter of 3.0 mm drill was used to make a bi-cortical channel to form a bone defect model accompanied with removing periosteum partially and prepared ice saline solution was irrigated to avoid thermal necrosis during the widened process. Then saline solution rinsed the drilled channel and they were treated with 2 mg mL^{-1} sCT or Gel randomly. The blank control group received no treatment.

Radiological Analysis: In order to evaluate the bone regeneration in vivo in different groups, the distal femurs were collected and scanned using an X-ray machine (Faxitron) and micro-CT (Scanco Medical; 70 kV, 130 µA) to evaluate the bone ingrowth at 12 weeks after the surgery. Data analysis including BMD, and bone tissue volume/total tissue volume (BV/TV) was measured by the Scanco software.

Histological Evaluation: At 8 weeks after the treatment, the femurs samples were fixed in 4% paraformaldehyde for 2 days, and then decalcified in 10% EDTA. After decalcifying for 8 weeks, the samples were embedded in paraffin blocks, and sectioned 5 µm thick for HE staining. Besides, immunohistochemical analysis was performed with antibodies against Col I (Abcam). The tissue changes in the bone defects under the different treatments were observed.

Statistical Analysis: All data were expressed as mean ± standard deviation. One-way analysis of variance (ANOVA) followed by Tukey's multiple comparison tests was executed. A p value of <0.05 was regarded as statistically significant.

Supporting Information

Supporting Information is available from the Wiley Online Library or from the author.

Acknowledgements

G.C. thanks the National Key Research and Development Program of China (2022YFB3800124) and NSFC/China (Nos. 52125303, 51721002, 91956127 and 21975047) for financial support. W.C. thanks National Key Research and Development Program of China (2020YFA0908200) and Shanghai Municipal Education Commission—Gaofeng Clinical Medicine Grant Support (20171906) for financial support. Y. Lu thank the Deutsche Forschungsgemeinschaft (DFG, German Research Foundation) - Project number 410871749 for financial support. The authors would like to thank the Joint Lab for Structural Research at the Integrative Research Institute for the Sciences (IRIS Adlershof, Berlin) for Cryo-EM imaging. This work is supported by Shanghai Municipal Science and Technology Major Project (No. 2018SHZDZX01) and ZJ Lab.

Conflict of Interest

The authors declare no conflict of interest.

Data Availability Statement

The data that support the findings of this study are available from the corresponding author upon reasonable request.

Keywords

active protein materials, bone regeneration, morphology manipulation

Received: August 18, 2022
Published online: October 9, 2022

---

[1] B. J. G. E. Pieters, M. B. van Eldijk, R. J. M. Nolte, J. Mecinović, *Chem. Soc. Rev.* **2016**, *45*, 24.
[2] N. P. King, Y. T. Lai, *Curr. Opin. Struct. Biol.* **2013**, *23*, 632.
[3] K. Matsuurua, *RSC Adv.* **2014**, *4*, 2942.
[4] Q. Luo, C. Hou, Y. Bai, R. Wang, J. Liu, *Chem. Rev.* **2016**, *116*, 13571.
[5] D. A. Silva, S. Yu, U. Y. Ulge, J. B. Spangler, K. M. Jude, C. Labão-Almeida, L. R. Ali, A. Quijano-Rubio, M. Ruterbusch, I. Leung, T. Biary, S. J. Crowley, E. Marcos, C. D. Walkey, B. D. Weitzner, F. Pardo-Avila, J. Castellanos, L. Carter, L. Stewart, S. R. Riddell, M. Pepper, G. J. L. Bernardes, M. Dougan, K. C. Garcia, D. Baker, *Nature* **2019**, *565*, 186.
[6] Y. Bai, Q. Luo, J. Liu, *Chem. Soc. Rev.* **2016**, *45*, 2756.
[7] Z. Li, S. Chen, C. Gao, Z. Yang, K.-C. Shih, Z. Kochovski, G. Yang, L. Gou, M.-P. Nieh, M. Jiang, L. Zhang, G. Chen, *J. Am. Chem. Soc.* **2019**, *141*, 19448.
[8] C. Gao, G. Chen, *Acc. Chem. Res.* **2020**, *53*, 740.
[9] N. M. Molino, S. W. Wang, *Curr. Opin. Biotechnol.* **2014**, *28*, 75.
[10] J. Bos, F. Fusetti, A. J. M. Driessen, G. Roelfes, *Angew. Chem., Int. Ed.* **2012**, *51*, 7472.
[11] D. Men, T.-T. Zhang, L.-W. Hou, J. Zhou, Z.-P. Zhang, Y.-Y. Shi, J.-L. Zhang, Z.-Q. Cui, J.-Y. Deng, D.-B. Wang, X.-E. Zhang, *ACS Nano* **2015**, *9*, 10852.
[12] J. A. Marsh, S. A. Teichmann, *Annu. Rev. Biochem.* **2015**, *84*, 551.
[13] Y. Zeng, M. Zhou, S. Mou, J. Yang, Q. Yuan, L. Guo, A. Zhong, J. Wang, J. Sun, Z. Wang, *J. Biomed. Mater. Res., Part A* **2020**, *108*, 2460.
[14] M. Diba, W. A. Camargo, M. Brindisi, K. Farbod, A. Klymov, S. Schmidt, M. J. Harrington, L. Draghi, A. R. Boccaccini, J. A. Jansen, J. J. J. P. van den Beucken, S. C. G. Leeuwenburgh, *Adv. Funct. Mater.* **2017**, *27*, 1703438.
[15] T.-L. Li, Z.-S. Tao, X.-j. Wu, M. Yang, H.-G. Xu, *J. Bone Miner. Metab.* **2021**, *39*, 934.
[16] C. T. Kao, Y. C. Chiu, A. K. X. Lee, Y. H. Lin, T. H. Huang, Y. C. Liu, M. Y. Shie, *Mater. Sci. Eng., C* **2021**, *119*, 111629.
[17] C. Dai, Y. Li, W. Pan, G. Wang, R. Huang, Y. Bu, X. Liao, K. Guo, F. Gao, *ACS Biomater. Sci. Eng.* **2020**, *6*, 575.
[18] H. D. Niall, H. T. Keutmann, D. H. Copp, J. T. Potrs, *Biochemistry* **1969**, *64*, 771.
[19] T. Seck, R. Baron, W. C. Horne, *J. Biol. Chem.* **2003**, *278*, 23085.
[20] T. J. Chambers, N. A. Athanasou, *J. Endocr.* **1984**, *102*, 281.
[21] H. M. Frost, *J. Bone Miner. Res.* **1999**, *14*, 1473.
[22] C. H. Chesnut, M. Azria, S. Silverman, M. Engelhardt, M. Olson, L. Mindeholm, *Osteoporosis Int.* **2008**, *19*, 479.
[23] M. C. Gaudiano, M. Colone, C. Bombelli, P. Chistolini, L. Valvo, M. Diociaiuti, *Biochim. Biophys. Acta, Proteins Proteomics* **2005**, *1750*, 134.
[24] G. Saito, J. A. Swanson, K.-D. Lee, *Adv. Drug Delivery Rev.* **2003**, *55*, 199.
[25] S. Ulrich, *Acc. Chem. Res.* **2019**, *52*, 510.
[26] N. D. Bansode, K. R. Sindhu, C. Morel, M. Rémy, J. Verget, C. Boiziau, P. Barthélémy, *Biomater. Sci.* **2020**, *8*, 3186.
[27] C. David, S. Foley, M. Enescu, *Phys. Chem. Chem. Phys.* **2009**, *11*, 2532.
[28] J. A. Burns, J. C. Butler, J. Moran, G. M. Whitesides, *J. Org. Chem.* **1991**, *56*, 2648.
[29] S.-L. Chang, G. A. Hofmann, L. Zhang, L. J. Deftos, A. K. Banga, *Int. J. Pharm.* **2000**, *200*, 107.
[30] D. Xie, M. Jiang, G. Zhang, D. Chen, *Chem. - Eur. J.* **2007**, *13*, 3346.
[31] K. Wei, L. Su, G. Chen, M. Jiang, *Polymer* **2011**, *52*, 3647.
[32] M. W. Jones, G. Mantovani, S. M. Ryan, X. Wang, D. J. Brayden, D. M. Haddleton, *Chem. Commun.* **2009**, 5272.
[33] J.-T. Yeon, K.-J. Kim, Y.-J. Son, S.-J. Park, S. H. Kim, *Arch. Pharmacal Res.* **2019**, *42*, 712.
[34] R. A. Davey, D. M. Findlay, *J. Bone Miner. Res.* **2013**, *28*, 973.